

Resolution and Robustness Bounds for Reconstructive Spectrometers

Changyan Zhu,^{1,2} Hsuan Lo,^{1,3} Jianbo Yu,⁴ Qijie Wang,⁴ and Y. D. Chong^{1,2}

¹*Division of Physics and Applied Physics, School of Physical and Mathematical Sciences, Nanyang Technological University, Singapore 637371*

²*Centre for Disruptive Photonic Technologies, Nanyang Technological University, Singapore 637371*

³*Department of Physics, Massachusetts Institute of Technology, Cambridge, Massachusetts 02139*

⁴*School of Electrical and Electronic Engineering, Nanyang Technological University, Singapore 637371*

Reconstructive spectrometers are a promising emerging class of devices that combine complex light scattering with inference to enable compact, high-resolution spectrometry. Thus far, the physical determinants of these devices' performance remain under-explored. We show that under a broad range of conditions, the noise-induced error for spectral reconstruction is governed by the Fisher information. We then use random matrix theory to derive a closed-form relation linking the variance bound to a set of key physical parameters: the spectral correlation length, the mean transmittance, and the number of frequency and measurement channels. The analysis reveals certain fundamental trade-offs between these physical parameters, and establishes the conditions for a spectrometer to achieve “super-resolution” below the limit set by the spectral correlation length. Our theory is confirmed using numerical validations with a random matrix model as well as full-wave simulations. These results establish a physically-grounded framework for designing and analyzing performant and noise-robust reconstructive spectrometers.

Introduction.—Spectrometers are a diverse class of devices that decompose light into its spectral constituents for analysis. They are traditionally divided into two types: dispersive spectrometers, which rely on geometric dispersion over long propagation paths, and interferometric spectrometers, which work by measuring optical path length differences [1]. Both approaches benefit from increased device size, and so face practical limits in miniaturization [2–4]. An alternative family of spectrometers, called reconstructive or computational spectrometers, has recently emerged [5–7]. While their individual designs vary widely, they typically encode the input light into a complex interference pattern, then use the measured pattern to infer the spectrum via some prior knowledge (e.g., data from a one-time calibration). Such schemes have been successfully used for spectrometry in the visible, infrared, and terahertz regimes, using disordered waveguides [2], multimode fibers [8, 9], colloidal quantum dots [10], and other platforms [11–13].

For conventional spectrometers, we have a sound understanding of how a device's performance depends on, and is limited by, its physical characteristics; for instance, one can deduce that the pixel-limited spectral resolution of a dispersive spectrometer scales as $1/L$, where L is the optical path length. For reconstructive spectrometers, however, the physical determinants of performance are less clear [14]. A commonly-cited heuristic is the spectral correlation length Γ_{corr} , i.e., the frequency scale over which the output patterns decorrelate [2, 6, 15, 16]. It seems reasonable that a short Γ_{corr} is desirable, as it makes the patterns for neighboring frequencies more easily distinguishable, but there have been only limited efforts to study this systematically [17]; it is unclear if Γ_{corr} is the main constraint, or whether other physical properties such as transmittance, noise levels, etc., may be more relevant. Moreover, the performance of a reconstructive

spectrometer may depend on idiosyncratic features of the reconstruction algorithm, such as domain-specific priors, which make it hard to draw general conclusions.

In this Letter, we develop a broadly-applicable figure of merit for the performance of a reconstructive spectrometer, and analyze its implications for the device's desired physical characteristics. We first abstract away most implementation details, retaining only the following assumptions: (i) the spectrum is inferred from light intensity measurements on a fixed set of output channels; (ii) each intensity measurement is subject to independent Gaussian noise; and (iii) there are no additional relevant priors about the spectrum (e.g., sparsity). The number of measurement channels may be smaller than the number of frequency channels, so that the inference problem is under-determined. Under these conditions, the theory of Fisher information [18] implies that the noise-induced reconstruction error is bounded below by $\sigma_\epsilon^2 \text{Tr}[(\mathbf{A}^T \mathbf{A})^+]$, where σ_ϵ is the noise level, \mathbf{A} is the normalized spectral transmission matrix, and $(\dots)^+$ denotes the Moore–Penrose pseudoinverse. By leveraging on empirically-grounded features of generic \mathbf{A} matrices [19–24], we derive expressions for the noise-induced reconstruction error and effective resolution in terms of Γ_{corr} , the average transmittance, and the number of frequency and measurement channels. In particular, our results clarify the necessary conditions for a reconstructive spectrometer to achieve “super-resolution” below the scale set by Γ_{corr} .

We subject the theory to two sets of numerical tests: a random matrix theory (RMT) model, and full-wave simulations. Over a wide range of conditions, the theoretical predictions closely match the actual error rates, either using the pseudoinverse or a neural network for inference. We also demonstrate that the super-resolution regime is achievable in both kinds of models. In the full-wave simulations, we show that combining our results

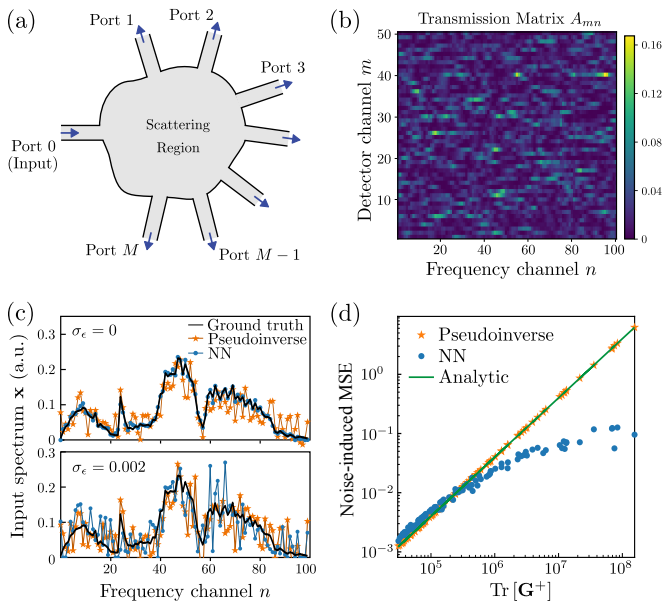


FIG. 1. (a) Schematic of a reconstructive spectrometer with M output ports. (b) Contents of a typical transmission matrix \mathbf{A} , of size $M = 50$ and $N = 100$, generated from the RMT model [19, 26]. Each of the N columns contains the output intensities at a given frequency. (c) Simulated spectral reconstruction under zero noise (upper panel) and noise level $\sigma_\epsilon = 0.002$ (lower panel). The ground truth (black line) is reconstructed via the transmission matrix from (b) using a pseudoinverse (orange stars), or a neural network (NN) trained on spectrum-intensity pairs (blue circles). (d) Noise-induced mean squared error (MSE) versus $\text{Tr}[\mathbf{G}^+]$, for an ensemble of \mathbf{A} matrices with $\sigma_\epsilon = 0.002$. The samples are generated by varying the RMT model’s coupling strength $\gamma \in [0.002, 0.01]$, keeping all other parameters constant [26].

with the scaling laws for diffusive transport [25] predicts an optimal device size without a brute-force search. Our theory thus yields useful insights to guide the design of reconstructive spectrometers.

Spectral Reconstruction Model.—A schematic of a reconstructive spectrometer is shown in Fig. 1(a). Light enters an input port (0), undergoes linear scattering, and partly exits through a set of output ports 1 to M . The system’s scattering matrix, $\mathbf{S}(\omega) \in \mathbb{C}^{(M+1) \times (M+1)}$, varies with frequency ω . We sample N equally-spaced frequencies $\omega_1, \dots, \omega_N$. The $M \times N$ spectral transmission matrix \mathbf{A} , defined by $A_{mn} = |S_{m0}(\omega_n)|^2 \in \mathbb{R}_0^+$, gives the intensity in each port and frequency channel. Fig. 1(b) shows a visualization of a typical \mathbf{A} matrix.

For an input with power spectrum $\mathbf{x} \in (\mathbb{R}_0^+)^N$, the output intensities are $\mathbf{y} \in (\mathbb{R}_0^+)^M$. We assume the measurements are subject to additive Gaussian noise,

$$\mathbf{y} = \mathbf{A}\mathbf{x} + \boldsymbol{\epsilon}, \quad \boldsymbol{\epsilon} \sim \mathcal{N}(\mathbf{0}, \sigma_\epsilon^2 \mathbf{1}_M), \quad (1)$$

where σ_ϵ is the noise level. Given \mathbf{y} , we aim to infer \mathbf{x} , which reduces to inverting \mathbf{A} if $\sigma_\epsilon = 0$ and $M = N$. From the log-likelihood $\log p(\mathbf{y}|\mathbf{x}) = -(M/2) \log(2\pi\sigma_\epsilon^2) -$

$(2\sigma_\epsilon^2)^{-1} \|\mathbf{y} - \mathbf{A}\mathbf{x}\|_2^2$, we can obtain the Fisher matrix [18]

$$\mathbb{E}[\nabla_{\mathbf{x}} \log p \nabla_{\mathbf{x}} \log p^\top] = \sigma_\epsilon^{-2} \mathbf{G}, \quad (2)$$

where $\mathbf{G} = \mathbf{A}^T \mathbf{A}$. By the Cramér–Rao lower bound, if $\hat{\mathbf{x}}$ is an unbiased estimator of \mathbf{x} , its covariance satisfies $\text{Cov}(\hat{\mathbf{x}}) \succeq \sigma_\epsilon^2 \mathbf{G}^+$, where $\mathbf{G}^+ \equiv \mathbf{G}^T (\mathbf{G} \mathbf{G}^T)^{-1}$ for $M < N$, and $\mathbf{G}^+ \equiv (\mathbf{G}^T \mathbf{G})^{-1} \mathbf{G}^T$ for $M \geq N$ [27, 28]. The bound is saturated by the least squares (or maximum-likelihood) estimator if \mathbf{A} has full column rank. The trace gives a scalar bound for the mean squared error (MSE); if $\hat{\mathbf{x}}$ is biased, this decomposes into an estimator variance and squared bias,

$$\mathbb{E} \|\hat{\mathbf{x}} - \mathbf{x}\|_2^2 \geq \sigma_\epsilon^2 \text{Tr}(\mathbf{G}^+) + \|\mathbb{E}[\hat{\mathbf{x}}] - \mathbf{x}\|_2^2. \quad (3)$$

To test this, we simulate spectral reconstruction with \mathbf{A} matrices derived from random \mathbf{S} matrices generated by the physically-motivated Mahaux–Weidenmüller model [19], and \mathbf{x} ’s derived from real spectra from the HITRAN dataset [29] (see the Supplemental Materials [26]). In Fig. 1(c), the upper panel shows a typical outcome with $M = 50$ ports, $N = 100$ frequency channels, and zero noise ($\sigma_\epsilon = 0$). Compared to the ground truth \mathbf{x} (black line), the pseudoinverse estimator $\hat{\mathbf{x}} = \mathbf{A}^+ \mathbf{y}$ is fairly accurate (orange stars). For comparison, we also train a dense neural network (NN) on a dataset of input-output pairs (see Supplemental Materials [26]); this nonlinear method, which falls outside the scope of the above analysis, yields comparable or better results (blue circles). Next, we add noise ($\sigma_\epsilon = 0.002$), and the revised results are shown in the lower panel of Fig. 1(c). Both the pseudoinverse and NN estimates undergo degradation, which can be quantified by the “noise-induced MSE”—i.e., the difference in MSE with and without noise, which is equivalent to subtracting the bias term in (3).

Fig. 1(d) shows the noise-induced MSE for 100 samples of \mathbf{A} , generated by varying the coupling strength in the RMT model and checking 500 test spectra for each \mathbf{A} . The predicted variation of the noise-induced MSE with $\text{Tr}(\mathbf{G}^+)$ is the green line, which the pseudoinverse results follow closely. For NN reconstruction, the noise-induced MSE initially follows the line, but falls below it at larger values of $\text{Tr}(\mathbf{G}^+)$, which may be due to the NN exploiting prior information about the spectra to mitigate the effects of noise more effectively. Overall, we conclude that the Cramér–Rao bound holds for both methods in the small $\text{Tr}(\mathbf{G}^+)$ regime, where noise is not dominant. The pseudoinverse and NN also behave differently with respect to the bias (i.e., non-noise-induced) part of the MSE, which is not shown in Fig. 1(d); the NN can attain a lower bias by learning the features of the spectra in the dataset. A detailed comparison, over a range of model parameters, is given in the Supplemental Materials [26].

Physical variables.—The Fisher information is an abstract quantity, so let us try to gain more insight into the above results by analyzing the contents of the \mathbf{A} matrix. Each of its columns, \mathbf{A}_n , can be decomposed as

$$\mathbf{A}_n = \langle \mathbf{A}_n \rangle + \mathbf{a}_n. \quad (4)$$

Defining also the mean-subtracted transmission matrix $\mathbf{a} = [\mathbf{a}_1, \dots, \mathbf{a}_N]$, we find that

$$\mathbf{A}^T \mathbf{A} = N \boldsymbol{\mu}^T \boldsymbol{\mu} + \mathbf{C}, \quad \text{where} \quad \begin{cases} \boldsymbol{\mu} \equiv \langle A_{mn} \rangle \mathbf{1}_M \\ \mathbf{C} \equiv \mathbf{a}^T \mathbf{a} \in \mathbb{R}^{N \times N}. \end{cases} \quad (5)$$

Note that the cross terms $\langle \mathbf{A}_n \rangle^T \mathbf{a}_{n'}$ vanish. By the Sherman–Morrison formula [30], the rank-1 term $N \boldsymbol{\mu}^T \boldsymbol{\mu}$ modifies the inverse matrix in the direction defined by $\boldsymbol{\mu}$. For large N , the trace of the inverse is dominated by the bulk spectrum of \mathbf{C} , so this shift is negligible, and

$$\text{Tr}[(\mathbf{A}^T \mathbf{A})^+] = \text{Tr}[(N \boldsymbol{\mu}^T \boldsymbol{\mu} + \mathbf{C})^+] \approx \text{Tr}[\mathbf{C}^+]. \quad (6)$$

Each element of \mathbf{C} is the inner product of two zero-mean vectors \mathbf{a}_i and \mathbf{a}_j . If we assume speckle statistics typical of chaotic scattering media (with intensities following a Rayleigh distribution, and the standard deviation of the transmission equaling the mean [31]), the correlations can be approximated as [26]

$$\text{corr}(\mathbf{A}_i, \mathbf{A}_j) = \frac{\langle \mathbf{a}_i, \mathbf{a}_j \rangle}{\|\mathbf{a}_i\| \|\mathbf{a}_j\|} \approx \frac{C_{ij}}{T_0^2}, \quad (7)$$

where $T_0 \equiv M \langle A_{mn} \rangle$ is the total transmittance from the input to all M outputs, averaged over all frequencies.

In many physical systems, spectral correlations decay with frequency separation (i.e., $|i - j|$ if the frequency channels are equally spaced) as Lorentzians [2, 20, 21, 32, 33]; for details, see the Supplemental Materials. If this feature holds, \mathbf{C} is a *near-Toeplitz* matrix, i.e., the expectation of $\mathbf{C} = \mathbb{E}[\mathbf{C}]$ takes a Toeplitz form [34]:

$$C_{ij} = T_0^2 \frac{a^2}{(i - j)^2 + a^2}, \quad a \equiv \frac{\Gamma_{\text{corr}}}{\Delta\omega}. \quad (8)$$

Here, $\Delta\omega$ is the sampling step in frequency space, and Γ_{corr} is the correlation length. Any single realization of the actual \mathbf{C} matrix fluctuates around this mean form, as shown in Fig. 2(a) for a sample drawn from the RMT model. The spectral correlation, shown in Fig. 2(b), exhibits a Lorentzian profile. To quantify this, we define the correlation length Γ_{corr} as the full width at half maximum (FWHM) of the spectral correlation. A theoretical Lorentzian curve is then generated based on this extracted Γ_{corr} value.

For large N , the generating function (i.e., dwell-time distribution) of such a matrix is asymptotically given by $f(\theta) = \sum_{k=-\infty}^{\infty} C_k e^{ik\theta}$, where $C_k = C_{|k|}$ [35]. Consider, for now, the over-determined regime ($M \geq N$). We can simplify $f(\theta)$ using the summation identity

$$\sum_{k=-\infty}^{\infty} \frac{e^{-ik\theta}}{k^2 + a^2} = \frac{\pi}{a \sinh(\pi a)} \cosh[a(\pi - |\theta|)], \quad (9)$$

along with Szegő's theorem [36], to obtain

$$\frac{1}{N} \text{Tr} \mathbf{C}^+ \xrightarrow{N \rightarrow \infty} \frac{1}{2\pi} \int_{-\pi}^{\pi} \frac{d\theta}{f(\theta)} = \frac{J(a)}{T_0^2}, \quad (10)$$

$$J(a) \equiv \frac{2 \sinh(\pi a)}{\pi a^2} \tan^{-1} \left[\tanh\left(\frac{\pi a}{2}\right) \right]. \quad (11)$$

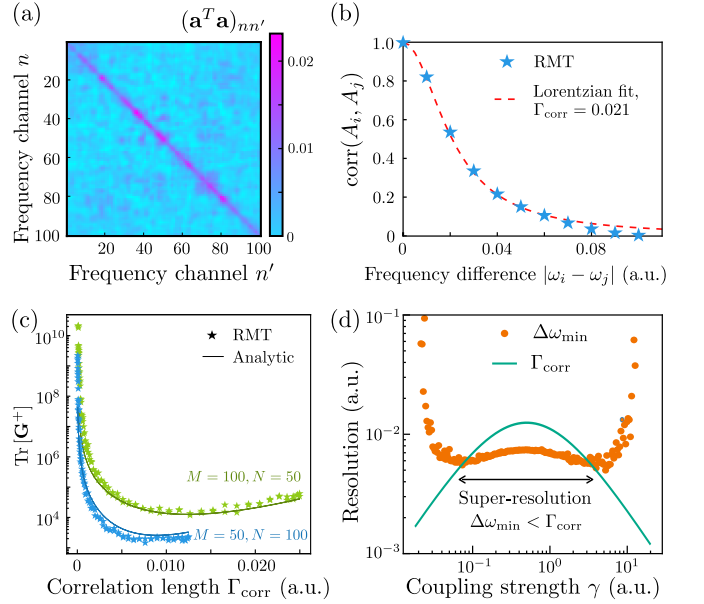


FIG. 2. (a) Structure of the matrix $\mathbf{C} = \mathbf{a}^T \mathbf{a}$ for a typical scatterer, showing its near-Toeplitz form. The \mathbf{A} matrix is generated by random matrix theory (RMT) using a Mahaux–Weidenmüller model [19]. (b) Calculated correlation function between columns of the \mathbf{A} matrix from (a), showing a Lorentzian decay with frequency spacing. The FWHM is denoted by Γ_{corr} . (c) Variation of $\text{Tr}[\mathbf{G}^+]$ with Γ_{corr} , using an RMT ensemble in which the coupling parameter γ varies from 0.005 to 0.1, with $N_{\text{modes}} = 500$ internal cavity modes. The results calculated directly from the \mathbf{A} matrices (stars) agree with the analytic results based on Γ_{corr} and the mean transmittance T_0 (solid curves), for both the under-determined and over-determined regimes. (d) Effective resolution $\Delta\omega_{\text{min}}$ and spectral correlation length Γ_{corr} versus coupling strength γ . Each data point is averaged over 200 samples, using $M = 50$, $N = 100$, and $N_{\text{modes}} = 500$. The effective resolution $\Delta\omega_{\text{min}}$ is calculated from Eq. (16) using $\delta_{\text{th}}^2 = 4 \times 10^{-4}$. Over a range of γ , the device exhibits super-resolution ($\Delta\omega_{\text{min}} < \Gamma_{\text{corr}}$).

Hence, we find

$$\mathbb{E}[\text{Tr}(\mathbf{G}^+)] = \frac{M}{|M - N|} \text{Tr} \mathbf{C}^+ = \frac{MN}{|M - N|} \frac{J(a)}{T_0^2}. \quad (12)$$

The $M/(M - N)$ factor arises from the Marchenko–Pastur distribution governing the spectrum of Wishart matrices; when $M \rightarrow N$, it diverges due to ill-conditioning [37] [38]. The normalized correlation length a , defined in Eq. (8), enters via $J(a)$. This function is monotonically-increasing, and in the limit of uncorrelated channels ($a < 1$) it has a minimum $J(0) \rightarrow \pi$, whereas for $a \gtrsim 1$ it has the asymptotic form $J(a) \approx e^{\pi a}/(4a^2)$ [26].

We can translate the result into an effective spectral resolution $\Delta\omega_{\text{min}}$, defined as the minimum frequency spacing to keep the reconstruction MSE below a threshold δ_{th}^2 . In the aforementioned correlated-channel regime

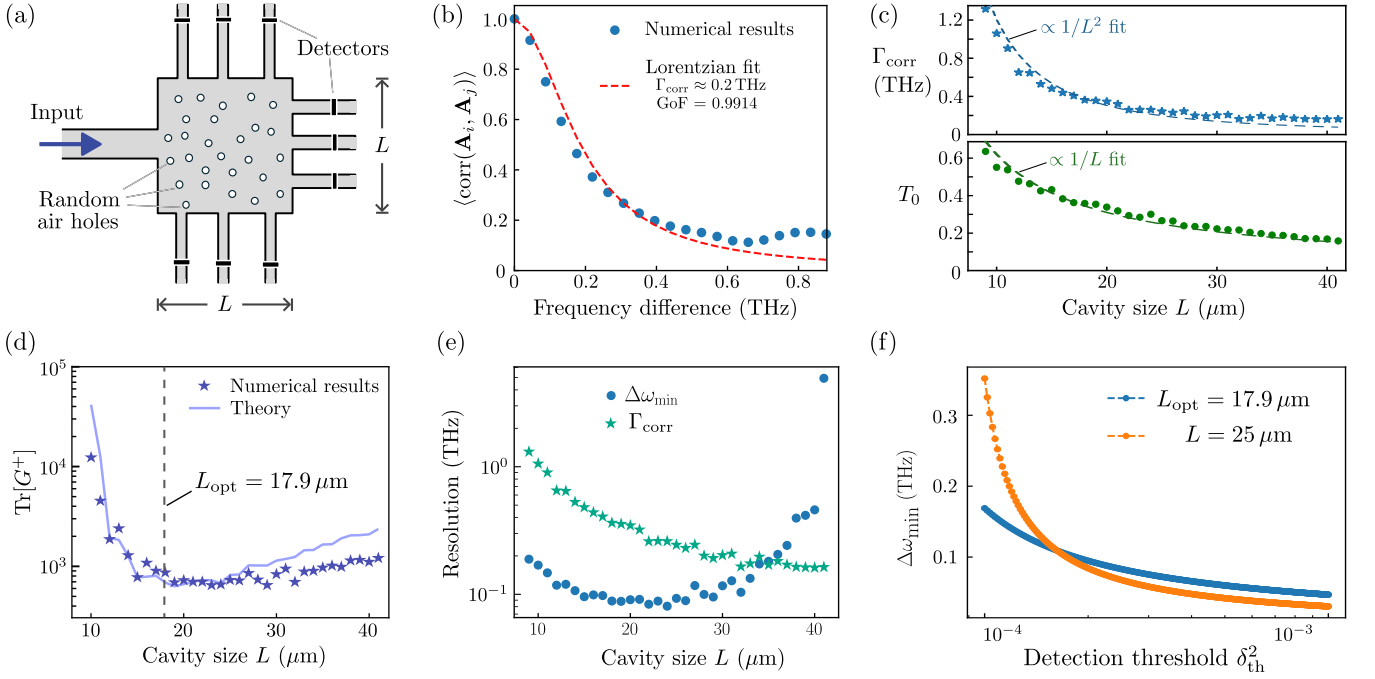


FIG. 3. (a) Schematic of the on-chip reconstructive spectrometer with a $L \times L$ scattering region. (b) Spectral correlation function from FDTD simulations for $L = 30 \mu\text{m}$ (blue circles), fitted to a Lorentzian (red dashes) to extract Γ_{corr} . (c) Scaling of Γ_{corr} (upper) and mean transmittance T_0 (lower) with cavity size L . Data points (averaged over 10 samples) agree well with the diffusive scaling laws $\Gamma_{\text{corr}} \propto L^{-2}$ and $T_0 \propto L^{-1}$ (dashed lines). (d) Reconstruction error metric $\text{Tr}[\mathbf{G}^+]$ versus L . The results obtained directly from the simulated \mathbf{A} matrices (blue stars) are close to the theoretical predictions based on Eq. (12) (blue line). The minimum of the latter matches the optimal cavity size L_{opt} derived from the fits in (c) (vertical dashes). (e) Plot of the effective resolution $\Delta\omega_{\text{min}}$ (orange circles) and Γ_{corr} (red circles) versus L , for detection threshold $\delta_{\text{th}}^2 = 2 \times 10^{-4}$ and noise level $\sigma_\epsilon = 10^{-2}$. (f) Effective resolution $\Delta\omega_{\text{min}}$ versus detection threshold δ_{th}^2 , using two choices of cavity size: $L_{\text{opt}} = 17.9 \mu\text{m}$ (blue circles), which minimizes $\text{Tr}[\mathbf{G}^+]$ as shown in (d); and $L = 25 \mu\text{m}$, which minimizes $\Delta\omega_{\text{min}}$ at $\delta_{\text{th}}^2 = 2 \times 10^{-4}$, as shown in (e). Here we again use $\sigma_\epsilon = 10^{-2}$.

($a \gtrsim 1$), we straightforwardly obtain

$$\Delta\omega_{\text{min}} \approx \frac{\pi\Gamma_{\text{corr}}}{\ln \mathcal{R}_{\text{SNR}}}, \quad \mathcal{R}_{\text{SNR}} \approx \delta_{\text{th}}^2 \frac{|M - N| T_0^2}{MN \sigma_\epsilon^2}, \quad (13)$$

where \mathcal{R}_{SNR} quantifies the effective signal-to-noise ratio. This implies that “super-resolution” below the scale of Γ_{corr} is possible, but requires \mathcal{R}_{SNR} to be large (e.g., by increasing T_0 or lowering σ_ϵ). This is a counterpart to the $1/L$ limit for conventional dispersive spectrometers.

In the under-determined case ($M < N$), \mathbf{G} is not full rank, but we find that the rank deficiency can be compensated by replacing $J(a)$ with

$$\tilde{J}(a) = \frac{2 \sinh(\sqrt{2} \frac{M}{N} \pi a)}{\pi a^2} \tan^{-1} \left[\tanh \left(\frac{\pi a}{2} \right) \right]. \quad (14)$$

For details, see the Supplemental Materials [26]. Therefore, Eq. (12) is replaced with

$$\mathbb{E} [\text{Tr}(\mathbf{G}^+)] \approx \frac{MN}{|M - N|} \frac{\tilde{J}(a)}{T_0^2}, \quad (15)$$

and the corresponding resolution in the $a \gg 1$ limit is

$$\Delta\omega_{\text{min}} \approx \frac{\sqrt{2}M}{N} \frac{\pi\Gamma_{\text{corr}}}{\ln \mathcal{R}_{\text{SNR}}}. \quad (16)$$

To test these results, we generate RMT samples with different values of the coupling strength γ , and observe how $\text{Tr}[\mathbf{G}^+]$ varies with the normalized correlation length a across this ensemble. As shown in Fig. 2(c), the numerical results are very close to the theoretical predictions for both the over-determined and under-determined regimes. Contrary to the common intuition that a short correlation length must be desirable [6, 15, 16], the reconstruction MSE varies non-monotonically with a . (Both a and T_0 vary with γ , leading to performance trade-offs as predicted by the theory.) In Fig. 2(d), we plot the effective resolution $\Delta\omega_{\text{min}}$ versus γ for the under-determined case ($M < N$), and find that the system can enter the super-resolution regime $\Delta\omega_{\text{min}} < \Gamma_{\text{corr}}$ in a certain interval of γ . This regime can also be reached by varying other parameters in the RMT model.

Full-wave simulations.—We now demonstrate that our theory can provide quantitative guidelines for designing realistic reconstructive spectrometers. We perform full-wave finite-difference time-domain (FDTD) simulations of the two-dimensional on-chip spectrometer structure shown in Fig. 3(a), similar to the design in Ref. [2]. The device comprises a square dielectric cavity of size $L \times L$, patterned with circular air holes (diameter $d_0 = 0.4 \mu\text{m}$)

in a Poisson-disk distribution with a mean spacing $d \approx 1.8d_0$. A transverse-electric Gaussian pulse (78.89–83.28 THz) is injected, and the scattered light is collected by $M = 9$ output waveguides. The spectral range is discretized into $N = 100$ channels to extract the transmission matrix \mathbf{A} . Fig. 3(b) shows the spectral correlation function for samples of size $L = 30 \mu\text{m}$, which exhibits a Lorentzian lineshape, consistent with our assumptions. We now systematically generate ensembles of \mathbf{A} by varying L (which serves as a proxy for the optical path length) from 10 to 40 μm , with all other parameters fixed.

Figure 3(c) shows how the scattering properties depend on L . Both T_0 and Γ_{corr} vary according to the scaling laws for diffusive transport: $T_0 \propto \ell/L$ and $\Gamma_{\text{corr}} \propto D/L^2$, where ℓ is the transport mean free path and D is the diffusion constant [25]. Using this, we can deduce the optimal cavity size without a brute-force search. We aim to minimize the reconstruction error $\mathcal{E}[a(L)] \propto \tilde{J}[a(L)]/a(L)$; solving $d\mathcal{E}/da = 0$ numerically for $M = 9$ and $N = 100$, using Eq. (14), yields $a_{\text{opt}} \approx 7.46$. Using the fitted diffusion constant $D \approx 120 \mu\text{m}^2/\text{THz}$ and frequency channel spacing $\Delta\omega = 0.0439 \text{ THz}$, we obtain an optimal cavity size $L_{\text{opt}} = \sqrt{D/(a_{\text{opt}} \cdot \Delta\omega)} \approx 17.9 \mu\text{m}$, matching the observed minimum of $\text{Tr}[\mathbf{G}^+]$ as shown in Fig. 3(d). This also illustrates a key trade-off highlighted by the theory: for $L < L_{\text{opt}}$, performance is limited by excessive spectral correlations, whereas for $L > L_{\text{opt}}$ it is limited by low optical throughput.

In Fig. 3(e), we plot the effective resolution $\Delta\omega_{\text{min}}$ and Γ_{corr} versus L . It can be seen that the spectrometer operates in the super-resolution regime below a certain cavity size, and the previously-obtained value of L_{opt} lies in this regime. Note that our previously-derived L_{opt} is near, but not equal to, the minimum of $\Delta\omega_{\text{min}}$ in this plot. These are two related but distinct design targets one has to choose between: the former maximizes the overall fidelity (by minimizing the noise-induced MSE), while the latter optimizes the effective frequency resolution at a given noise level and detection threshold. To clarify this, Fig. 3(f) shows the effective resolution $\Delta\omega_{\text{min}}$ versus detection threshold δ_{th}^2 for two cavity sizes: (i) $L = L_{\text{opt}}$, and (ii) $L = 25 \mu\text{m}$, where the resolution curve in Fig. 3(e) reaches its minimum. The latter indeed yields a finer spectral resolution when operating at $\delta_{\text{th}}^2 = 2 \times 10^{-4}$, the detection threshold used in Fig. 3(e);

for smaller δ_{th}^2 , it gives a *worse* (i.e., larger) resolution.

Conclusions.—The performance of a reconstructive spectrometer is largely determined by the variance bound $\text{Tr}[\mathbf{G}^+]$, derived from its spectral transmission matrix. When noise is present but non-dominant, this quantity accurately describes the noise-induced error for not only pseudoinverse-based reconstruction, but also inference using a neural network, implying that the criterion is reasonably algorithm-independent. We have derived expressions for $\text{Tr}[\mathbf{G}^+]$, and hence the effective frequency resolution, in terms of physically meaningful variables: the spectral correlation length Γ_{corr} , mean transmittance T_0 , the number of intensity measurement channels, etc. The theory yields successful predictions for both RMT models and a full-wave simulation of an on-chip device. The tests confirm that Γ_{corr} is not the sole determinant of performance for a reconstructive spectrometer; notably, T_0 also plays a role and can lead to a trade-off.

A key assumption we have made is that the scatterer exhibits conventional speckle statistics with Lorentzian spectral correlations [20, 21, 32, 33]. This assumption holds for almost all scattering-based reconstructive spectrometers implemented to date, including those based on photonic chips [2], multimode fibers [8], colloids [10], and nanostructures [12, 13]—but it is not a universal law. In the Supplemental Materials [26], we demonstrate that when a scatterer is expressly inverse-designed [39, 40] to minimize $\text{Tr}[\mathbf{G}^+]$ [41], the generated structure eventually acquires highly non-Lorentzian correlations while also surpassing the performance predicted by our theory. This hints that non-Lorentzian speckle statistics, which have previously been studied in the context of fundamental wave physics [42, 43], may have an important application in this area. In future, it will be desirable to find additional theoretical techniques to model such systems, such as the extremal statistics of RMT models [42], which would allow us to characterize the ultimate limits of reconstructive spectrometry.

We thank A. Nussupbekov, B. Zhu, F. J. N. Jorgensen, and S. G. Johnson for helpful discussions. This work was supported by the Singapore National Research Foundation (NRF) under the NRF Investigatorship NRF-NRFI08-2022-0001, and Competitive Research Program (CRP) Nos. NRF-CRP23-2019-0005, NRF-CRP23-2019-0007, and NRF-CRP29-2022-0003.

[1] S. P. Davis, M. C. Abrams, and J. W. Brault, *Fourier transform spectrometry* (Academic press, 2001).
 [2] B. Redding, S. F. Liew, R. Sarma, and H. Cao, Compact spectrometer based on a disordered photonic chip, *Nature Photonics* **7**, 746 (2013).
 [3] B. Momeni, E. S. Hosseini, M. Askari, M. Soltani, and A. Adibi, Integrated photonic crystal spectrometers for sensing applications, *Optics communications* **282**, 3168 (2009).
 [4] Z. Xia, A. A. Eftekhar, M. Soltani, B. Momeni, Q. Li,

M. Chamanzar, S. Yegnanarayanan, and A. Adibi, High resolution on-chip spectroscopy based on miniaturized microdonut resonators, *Optics express* **19**, 12356 (2011).
 [5] T. Yang, C. Xu, H.-p. Ho, Y.-y. Zhu, X.-h. Hong, Q.-j. Wang, Y.-c. Chen, X.-a. Li, X.-h. Zhou, M.-d. Yi, *et al.*, Miniature spectrometer based on diffraction in a dispersive hole array, *Optics letters* **40**, 3217 (2015).
 [6] Z. Yang, T. Albrow-Owen, W. Cai, and T. Hasan, Miniaturization of optical spectrometers, *Science* **371**, eabe0722 (2021).

- [7] L. Zhang, J. Chen, C. Ma, W. Li, Z. Qi, and N. Xue, Research progress on on-chip fourier transform spectrometer, *Laser & Photonics Reviews* **15**, 2100016 (2021).
- [8] B. Redding and H. Cao, Using a multimode fiber as a high-resolution, low-loss spectrometer, in *Fiber Optic Sensors and Applications XI*, Vol. 9098 (SPIE, 2014) pp. 89–93.
- [9] S. F. Liew, B. Redding, M. A. Choma, H. D. Tagare, and H. Cao, Broadband multimode fiber spectrometer, *Optics letters* **41**, 2029 (2016).
- [10] J. Bao and M. G. Bawendi, A colloidal quantum dot spectrometer, *Nature* **523**, 67 (2015).
- [11] M. Faraji-Dana, E. Arbabi, A. Arbabi, S. M. Kamali, H. Kwon, and A. Faraon, Compact folded metasurface spectrometer, *Nature communications* **9**, 4196 (2018).
- [12] Z. Yang, T. Albrow-Owen, H. Cui, J. Alexander-Webber, F. Gu, X. Wang, T.-C. Wu, M. Zhuge, C. Williams, P. Wang, *et al.*, Single-nanowire spectrometers, *Science* **365**, 1017 (2019).
- [13] D.-G. Lee, G. Song, C. Lee, C. Lee, and M. Jang, Reconstructive spectrometer using double-layer disordered metasurfaces, *Science Advances* **11**, eadv2376 (2025).
- [14] D. A. Miller, Waves, modes, communications, and optics: a tutorial, *Advances in Optics and Photonics* **11**, 679 (2019).
- [15] H. H. Yoon, H. A. Fernandez, F. Nigmatulin, W. Cai, Z. Yang, H. Cui, F. Ahmed, X. Cui, M. G. Uddin, E. D. Minot, *et al.*, Miniaturized spectrometers with a tunable van der waals junction, *Science* **378**, 296 (2022).
- [16] G. Cai, Y. Li, Y. Zhang, X. Jiang, Y. Chen, G. Qu, X. Zhang, S. Xiao, J. Han, S. Yu, *et al.*, Compact angle-resolved metasurface spectrometer, *Nature Materials* **23**, 71 (2024).
- [17] P. Varytis, D.-N. Huynh, W. Hartmann, W. Pernice, and K. Busch, Design study of random spectrometers for applications at optical frequencies, *Optics Letters* **43**, 3180 (2018).
- [18] B. R. Frieden, *Physics from Fisher information: a unification* (Cambridge University Press, 1998).
- [19] Y. V. Fyodorov, Random matrix theory of resonances: An overview, in *2016 URSI International Symposium on Electromagnetic Theory (EMTS)* (IEEE, 2016) pp. 666–669.
- [20] N. Lehmann, D. Saher, V. Sokolov, and H.-J. Sommers, Chaotic scattering: the supersymmetry method for large number of channels, *Nuclear Physics A* **582**, 223 (1995).
- [21] Y. V. Fyodorov and H.-J. Sommers, Statistics of resonance poles, phase shifts and time delays in quantum chaotic scattering: Random matrix approach for systems with broken time-reversal invariance, *Journal of Mathematical Physics* **38**, 1918 (1997).
- [22] S. M. Popoff, G. Lerosey, R. Carminati, M. Fink, A. C. Boccarda, and S. Gigan, Measuring the transmission matrix in optics: An approach to the study and control of light propagation in disordered media, *Physical review letters* **104**, 100601 (2010).
- [23] A. Goetschy and A. Stone, Filtering random matrices: the effect of incomplete channel control in multiple scattering, *Physical review letters* **111**, 063901 (2013).
- [24] H. Cao and J. Wiersig, Dielectric microcavities: Model systems for wave chaos and non-hermitian physics, *Reviews of Modern Physics* **87**, 61 (2015).
- [25] E. Akkermans and G. Montambaux, *Mesoscopic physics of electrons and photons* (Cambridge university press, 2007).
- [26] See supplementary material (2025), see online Supplemental Materials.
- [27] S. M. Kay, *Fundamentals of statistical signal processing: estimation theory* (Prentice-Hall, Inc., 1993).
- [28] R. J. Ober, Q. Zou, and Z. Lin, Calculation of the fisher information matrix for multidimensional data sets, *IEEE transactions on signal processing* **51**, 2679 (2003).
- [29] L. S. Rothman, R. R. Gamache, A. Goldman, L. R. Brown, R. A. Toth, H. M. Pickett, R. L. Poynter, J.-M. Flaud, C. Camy-Peyret, A. Barbe, *et al.*, The hitran database: 1986 edition, *Applied optics* **26**, 4058 (1987).
- [30] J. Sherman and W. J. Morrison, Adjustment of an inverse matrix corresponding to a change in one element of a given matrix, *The Annals of Mathematical Statistics* **21**, 124 (1950).
- [31] J. W. Goodman, *Speckle phenomena in optics: theory and applications* (Roberts and Company Publishers, 2007).
- [32] T. Ericson, Fluctuations of nuclear cross sections in the "continuum" region, *Physical Review Letters* **5**, 430 (1960).
- [33] H. Weidenmüller and G. Mitchell, Random matrices and chaos in nuclear physics: Nuclear structure, *Reviews of Modern Physics* **81**, 539 (2009).
- [34] R. M. Gray *et al.*, Toeplitz and circulant matrices: A review, *Foundations and Trends in Communications and Information Theory* **2**, 155 (2006).
- [35] A. Böttcher and B. Silbermann, *Analysis of Toeplitz operators* (Springer, 2006).
- [36] I. Hirschman Jr, The strong szegő limit theorem for toeplitz determinants, *American Journal of Mathematics* , 577 (1966).
- [37] Strictly speaking, the scattering matrices in the Mahaux–Weidenmüller model are not Wishart, but they approximately satisfy Wishart statistics in the chaotic regime with strong mode overlap.
- [38] A. M. Tulino, S. Verdú, *et al.*, Random matrix theory and wireless communications, *Foundations and Trends in Communications and Information Theory* **1**, 1 (2004).
- [39] S. Molesky, Z. Lin, A. Y. Piggott, W. Jin, J. Vucković, and A. W. Rodriguez, Inverse design in nanophotonics, *Nature Photonics* **12**, 659 (2019).
- [40] S. Kroker, S. Lanteri, O. Miller, J. Niegemann, and L. Ramunno, Inverse design in photonics: introduction, *J. Opt. Soc. Am. B* **41**, IDP1 (2024).
- [41] J. Yu, H. Lo, W. Chen, C. Zhu, Y. Wu, F. Wang, C. Wang, C. Yan, C. Dang, B. Wen, *et al.*, Wavelength-scale noise-resistant on-chip spectrometer, *arXiv preprint arXiv:2509.22286* (2025).
- [42] A. Lakshminarayan, S. Tomsovic, O. Bohigas, and S. N. Majumdar, Extreme statistics of complex random and quantum chaotic states, *Phys. Rev. Lett.* **100**, 044103 (2008).
- [43] A. Chabanov, M. Stoytchev, and A. Genack, Statistical signatures of photon localization, *Nature* **404**, 850 (2000).

Supplemental Materials for
“Performance Bounds for Reconstructive Spectrometers”

S1. DATASET PREPARATION AND RECONSTRUCTION ALGORITHMS

Dataset preparation—In our numerical simulations, the ground truth spectrum samples are drawn from a dataset constructed from the HITRAN (High-Resolution Transmission) spectroscopic database [29]. From the database, we extract absorption spectra within the wavelength range 3600-3800 nm (78.9–83.3THz), selecting 64 experimental spectra corresponding to different isotopologues from 55 distinct molecules. Each spectrum is normalized to unit peak intensity and resampled onto a fixed frequency grid. We then generate synthetic spectra emulating mixtures that may be encountered in sensing applications, by randomly combining 2–5 distinct experimental spectra per sample. This procedure yields a dataset of 10^4 samples, of which 9000 are used for training the neural networks (see below), and 1000 for testing.

Reconstruction algorithms—During our numerical tests, we evaluate two spectral reconstruction algorithms:

1. The Moore-Penrose pseudoinverse. The estimator is $\hat{x} = A^+y$, where $A^+ = A^T(AA^T)^{-1}$. This linear reconstruction scheme serves as the baseline for the theoretical analysis based on Fisher information and the Cramér-Rao bound.
2. A fully-connected neural network (NN), implemented using the PyTorch framework. The NN comprises three hidden layers of 500 neurons each. Each layer is followed by a ReLU activation, dropout regularization, and batch normalization to enhance training stability and mitigate overfitting. Training is done using the Adam optimizer with a learning rate of 1×10^{-3} for 200 epochs; the loss function is the mean squared error (MSE) between the predicted and true spectra. Hyperparameters are optimized via grid search to achieve the best performance on a validation set.

S2. RMT SIMULATIONS

To model an ensemble of generic scatterers, we use a random matrix theory (RMT) model based on the Mahaux-Weidenmüller formalism [19]. A cavity is described by a $P \times P$ Hamiltonian \mathbf{H} sampled from the Gaussian unitary ensemble (GUE), and its coupling to $M + 1$ external channels is characterized by a $P \times (M + 1)$ random matrix \mathbf{W} , where

$$W_{pm} \sim \mathcal{N}(0, \gamma^2), \quad \gamma \in \mathbf{R}^+. \quad (\text{S1})$$

The scattering matrix is then given by

$$\mathbf{S}(\omega) = \mathbf{I} - i\mathbf{W}^+(\omega - \mathbf{H}_{\text{eff}})^{-1}\mathbf{W}, \quad (\text{S2})$$

$$\mathbf{H}_{\text{eff}} = \mathbf{H} - \frac{i}{2}\mathbf{W}\mathbf{W}^+, \quad (\text{S3})$$

where ω is the frequency. After sampling \mathbf{S} , we can generate the spectral transmission matrix \mathbf{A} , which has size $M \times N$ and is defined by $A_{mn} = |S_{m0}(\omega_n)|^2$, where $\omega_1, \dots, \omega_N$ are a set of equally-spaced discrete frequency channels.

Next, we apply these RMT samples to the spectra and reconstruction schemes described in Section S1. As noted in the main text, the reconstruction MSE can be decomposed into two terms, a noise-induced term and a bias term:

$$\mathbb{E} \|\hat{\mathbf{x}} - \mathbf{x}\|_2^2 \geq \sigma_\epsilon^2 \text{Tr}(\mathbf{G}^+) + \|\mathbb{E}[\hat{\mathbf{x}}] - \mathbf{x}\|_2^2. \quad (\text{S4})$$

We will analyze each term separately.

Noise-induced MSE—In Fig. S1a–c, we present simulation results showing the noise-induced MSE (i.e., the difference in MSE with and without noise) versus $\text{Tr}[\mathbf{G}^+]$, for different choices of RMT parameters. Within each subplot, we draw different ensembles by varying the RMT coupling parameter γ defined in Eq. (S1). The different subplots show different choices of the M (the number of measurement channels), with a fixed number of frequency channels $N = 100$. In each of the subplots—(a) the under-determined regime $M < N$, (b) $M = N$, and (c) the over-determined regime $M > N$ —we find that the noise-induced MSE for the pseudoinverse closely follows the prediction of $\sigma_\epsilon^2 \text{Tr}[\mathbf{G}^+]$ derived from the Cramér-Rao lower bound. The results for NN reconstruction follow a similar trend, with MSE

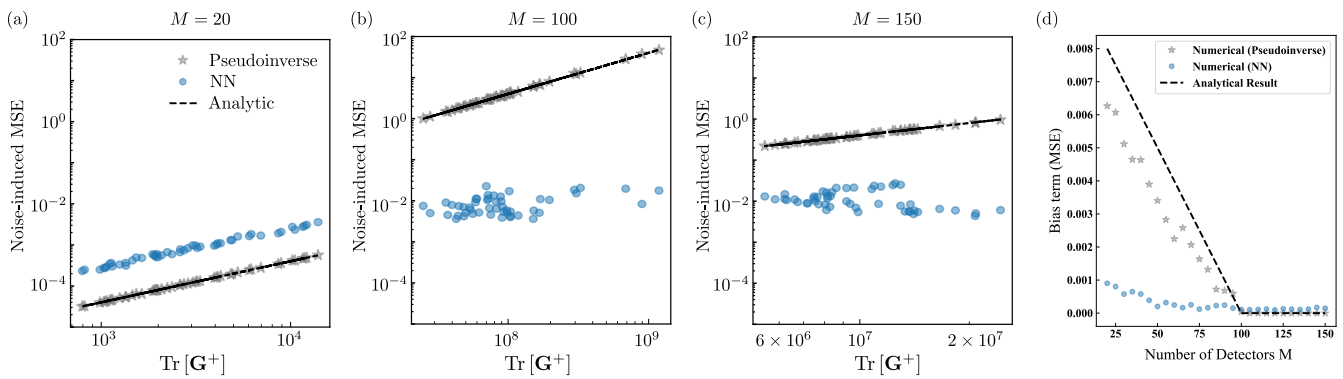


FIG. S1. (a)–(c) Noise-induced MSE versus $\text{Tr}[\mathbf{G}^+]$, obtained from RMT simulations with pseudoinverse and NN reconstruction schemes. Each data point is an ensemble average over fixed RMT parameters; the different subplots correspond to different $M \in \{20, 100, 150\}$, with fixed $N = 100$, and in each subplot we vary $\gamma \in [0.005, 0.01]$. The number of cavity modes is $P = 500$. The dashes show the Cramér–Rao bound $\sigma_\epsilon^2 \text{Tr}(\mathbf{G}^+)$, which quantitatively fits the pseudoinverse results. (d) Bias term for different M , with $N = 100$, $\gamma = 0.005$ and all other parameters the same as in (a)–(c). The pseudoinverse-based reconstruction experiences significantly increasing bias as M is decreased below N ; for NN reconstruction, the bias increases less sharply.

increasing with $\text{Tr}[\mathbf{G}^+]$. However, we observe deviations from linearity at higher values of $\text{Tr}[\mathbf{G}^+]$, indicating a more complex relationship than is captured by the Cramér–Rao theory.

Bias term.—Figure S1(d) plots the bias term, representing the intrinsic reconstruction error in the noise-free limit. This error arises solely from the projection of the signal \mathbf{x} onto the $(N - M)$ -dimensional null space of \mathbf{A} , which cannot be inverted linearly. Mathematically, the bias for the pseudoinverse estimator is given by $\text{Tr}[(\mathbf{I} - \mathbf{A}^+ \mathbf{A}) \mathbf{R}_{xx}]$, where $\mathbf{R}_{xx} = \mathbb{E}[\mathbf{x}\mathbf{x}^T]$ is the correlation matrix of the input spectra. For a random scattering matrix, the null space orientation is isotropic. Consequently, the bias is determined by the trace of the correlation matrix (total energy) scaled by the dimensionality reduction ratio:

$$\text{MSE}_{\text{bias}} \approx \frac{N - M}{N} \cdot \frac{\text{Tr}(\mathbf{R}_{xx})}{N} = \left(1 - \frac{M}{N}\right) \langle x^2 \rangle. \quad (\text{S5})$$

Conversely, in the over-determined regime ($M \geq N$), the null space vanishes, and the bias term becomes strictly zero. The analytical prediction (dashed line), calculated using the empirical second moment $\langle x^2 \rangle \approx 0.01$, captures this behavior perfectly, including the linear descent and the sharp transition to zero at $M = 100$. Notably, the Neural Network reconstruction (blue circles) yields a significantly lower bias than the linear baseline in the under-determined region, indicating that the model successfully leverages learned spectral priors to recover information within the null space.

S3. DETAILS OF SPECTROMETER RESOLUTION DERIVATION

Here, we present further details about the derivation leading to the results, given in the main text, for $\mathbb{E}[\text{Tr}(\mathbf{G}^+)]$ and the effective spectrometer resolution.

First, we discuss the approximation leading up to Eq. (7) in the main text, which simplifies the normalization factor in the correlation coefficient by a replacement

$$\|\mathbf{a}_i\| \|\mathbf{a}_j\| \rightarrow (\dots) T_0^2.$$

In the strong scattering regime characterized by the GOE or GUE ensembles, the complex scattering coefficients S_{m0} follow a circular complex Gaussian distribution [20, 21]. Consequently, the transmission intensities $A_{mn} = |S_{m0}(\omega_n)|^2$ follow a negative exponential (Rayleigh) distribution:

$$P(A) = \frac{1}{T_0} \exp\left(-\frac{A}{T_0}\right), \quad (\text{S6})$$

where $T_0 = \langle A_{mn} \rangle$ is the mean transmittance. This distribution has the property that the standard deviation equals the mean: $\sigma_A = T_0$. This justifies the approximation we used in the main text; specifically, the L_2 norm of the

zero-mean fluctuation vector \mathbf{a}_j scales with the standard deviation as

$$\|\mathbf{a}_j\| \approx \sqrt{M}\sigma_A = \sqrt{MT_0} \quad (\text{S7})$$

$$\Rightarrow \|\mathbf{a}_i\|\|\mathbf{a}_j\| \approx MT_0^2. \quad (\text{S8})$$

Since the covariance matrix C_{ij} scales with M (due to the inner product of vectors of length M), the normalized correlation can be approximated by C_{ij}/T_0^2 (absorbing M into the definition of C_{ij} as per standard RMT convention).

Next, we discuss why the spectral correlation function has a Lorentzian form, as stated in Eq. (8) of the main text. We work in the Ericson regime (strongly overlapping resonances), i.e., $\Gamma \gg \Delta$ where Δ is the mean level spacing, and Γ is the mean resonance width. In this regime, spectral averages are equivalent to ensemble averages due to the property of self-averaging (ergodicity) [32, 33]. The Weisskopf-Wigner result of RMT states that the survival (dwell-time) distribution of modes in the cavity is exponential:

$$P(t) = \frac{1}{\tau_d} e^{-t/\tau_d}, \quad \Gamma_W \equiv \frac{1}{\tau_d} = \frac{\Delta}{2\pi} \sum_{c=1}^M T_0. \quad (\text{S9})$$

Here, T_0 are the channel transmission coefficients.

Let $E_m(E)$ denote the complex field on detector pixel m . The first-order (mutual) field correlation for an energy offset ϵ is the Fourier transform of $P(t)$:

$$G_1^{(m)}(\epsilon) \equiv \langle E_m(E) E_m^*(E + \epsilon) \rangle \quad (\text{S10})$$

$$= \int_0^\infty P(t) e^{i\epsilon t} dt \quad (\text{S11})$$

$$= \frac{1}{1 - i\epsilon\tau_d}. \quad (\text{S12})$$

Hence, the normalized intensity correlation function is a Lorentzian:

$$|G_1^{(m)}(\epsilon)|^2 = \frac{1}{1 + (\epsilon\tau_d)^2} = \frac{\Gamma_{\text{corr}}^2}{\epsilon^2 + \Gamma_{\text{corr}}^2}, \quad (\text{S13})$$

where

$$\Gamma_{\text{corr}} \equiv 1/\tau_d = \Gamma_W. \quad (\text{S14})$$

S4. CORRELATION LENGTH FOR UNDER-DETERMINED SYSTEMS

Here, we derive the modified scaling function $\tilde{J}(a)$ given in Eq. (14) of the main text. This function is used in the under-determined regime ($M < N$) of the reconstructive spectrometer. For later convenience, let us define

$$\beta = M/N < 1. \quad (\text{S15})$$

In this regime, the Gram matrix $\mathbf{G} = \mathbf{A}^T \mathbf{A}$ can be viewed as a Toeplitz matrix generated by a $f(\theta)$ that has been modified by the finite observation window.

Mathematically, the entries of \mathbf{G} are formed by the autocorrelation of the transmission amplitudes over a finite window of size M . In the spectral domain (the domain of f), this finite windowing corresponds to a convolution of the asymptotic Lorentzian symbol $f_{\text{Lorentz}}(\theta)$ with the Fejér kernel $F_M(\theta)$:

$$\tilde{f}(\theta) = (f_{\text{Lorentz}} * F_M)(\theta) = \int_{-\pi}^{\pi} f_{\text{Lorentz}}(\phi) F_M(\theta - \phi) d\phi, \quad (\text{S16})$$

where

$$F_M(\theta) = \frac{1}{M} \frac{\sin^2(M\theta/2)}{\sin^2(\theta/2)} \quad (\text{S17})$$

is the spectral representation of the Bartlett (triangular) lag window.

Let us note that $\text{Tr}(\mathbf{G}^+)$ is dominated by the behavior of $\tilde{f}(\theta)$ near its global minimum (the spectral gap). The convolution with the Fejér kernel has two competing effects on the effective spectral correlation length a_{eff} that governs this minimum:

- *Linear Geometric Scaling*—The reduction in the number of independent measurement channels from N to M effectively compresses the frequency axis relative to the integration time. To first order, this suggests a rescaling of the correlation parameter $a \rightarrow \beta a$.
- *Spectral Broadening*—The convolution with the Fejér kernel (which has a main lobe width $\sim 4\pi/M$) smears out the sharp features of the Lorentzian symbol. This smoothing lifts the minimum of the symbol and broadens the spectral valley, increasing the correlation length relative to pure linear scaling.

To capture both effects analytically, we introduce the following ansatz for the effective correlation length a_{eff} in the modified trace formula:

$$a_{eff} = \eta\beta a. \quad (\text{S18})$$

Here, β accounts for the geometric reduction of dimensionality, and $\eta > 1$ is a shape correction factor accounting for the Fejér broadening. Let us now refer to the definition of the $J(a)$ function in Eq. (11) of the main text, reproduced here for convenience:

$$J(a) \equiv \frac{2 \sinh(\pi a)}{\pi a^2} \tan^{-1} \left[\tanh\left(\frac{\pi a}{2}\right) \right]. \quad (\text{S19})$$

We seek a form

$$\tilde{J}(a) \approx \frac{2 \sinh(\pi a_{eff})}{\pi a^2}. \quad (\text{S20})$$

By comparing to the RMT ensemble in the limit of strong correlations ($a \gg 1$), we find that the broadening factor converges to $\eta \approx \sqrt{2}$ —i.e., the Bartlett windowing broadens the effective spectral correlation width by a factor of $\sqrt{2}$ relative to a hard rectangular truncation. Thus, we set $a_{eff} = \sqrt{2} \frac{M}{N} a$. Substituting this into (S19) yields

$$\tilde{J}(a) = \frac{2 \sinh\left(\sqrt{2} \frac{M}{N} \pi a\right)}{\pi a^2} \tan^{-1} \left[\tanh\left(\frac{\pi a}{2}\right) \right]. \quad (\text{S21})$$

The pre-factor $1/(\pi a^2)$ and the \tan^{-1} term remain dependent on the original a as they relate to the normalization of the total energy and the bulk spectrum, which are less sensitive to the edge smoothing effects than the exponential tail governed by the sinh term.

S5. THE PROPERTIES OF THE INVERSE TRACE FORMULA

Here, we discuss the $J(a)$ function given in Eq. (12), which plays a central role in our results for the spectrometer's performance. In the limit where the spectral correlation length is much smaller than the sampling interval ($\Gamma_{corr} \ll \Delta\omega$), the system acts as a spectrometer with independent, uncorrelated channels (the "white" channel limit). Applying the small-angle approximations $\sinh(x) \approx x$ and $\tan^{-1}(\tanh(x)) \approx x$, we find:

$$\lim_{a \rightarrow 0} J(a) \approx \frac{2(\pi a)}{\pi a^2} \cdot \left(\frac{\pi a}{2}\right) = \pi. \quad (\text{S22})$$

Thus, we obtain:

$$\mathbb{E}[\text{Tr}(\mathbf{G}^+)] \propto \frac{MN}{|M - N|} \frac{\pi}{T_0}. \quad (\text{S23})$$

This recovers the fundamental noise floor for a reconstructive spectrometer with orthogonal transmission columns (i.e., uncorrelated measurements), consistent with standard RMT predictions for Wishart matrices [38]. In this case, the reconstruction error is mainly dependent on the mean transmittance T_0 . The spectral correlation length Γ_{corr} does not contribute to the error, as the channels are effectively independent.

Next, let us consider the highly correlated regime ($a \gtrsim 1$). This corresponds to the spectral correlation length far exceeding the channel spacing ($\Gamma_{corr} \gg \Delta\omega$), meaning that the transmission matrix is ill-conditioned (i.e., adjacent columns become nearly collinear). Using the approximation $\sinh(\pi a) \approx \frac{1}{2} e^{\pi a}$ and noting that $\tanh(\frac{\pi a}{2}) \rightarrow 1$ (implying $\tan^{-1}(1) = \pi/4$), we obtain

$$J(a) \approx \frac{e^{\pi a}}{\pi a^2} \cdot \frac{\pi}{4} = \frac{e^{\pi a}}{4a^2}. \quad (\text{S24})$$

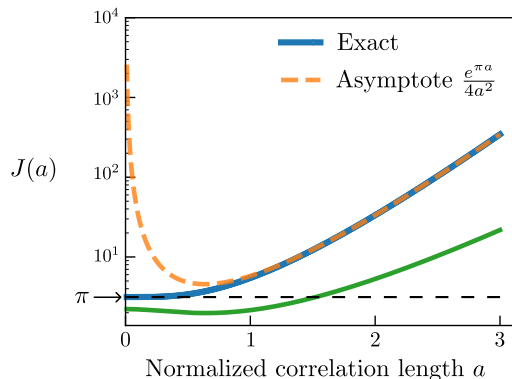


FIG. S2. Variation of the scaling function $J(a)$ with the normalized correlation length $a = \Gamma_{\text{corr}}/\Delta\omega$. The solid blue line represents the exact analytical form for the over-determined case ($M \geq N$), which converges to the asymptotic exponential behavior $\sim e^{\pi a}$ (orange dashed line) for large correlations. The green solid line depicts the modified function $\tilde{J}(a)$ for an under-determined system ($M/N = 0.5$), exhibiting suppressed error growth due to spectral smoothing. All functions converge to π at $a = 0$, representing the baseline error for uncorrelated channels.

This exponential growth in $J(a)$ indicates that the reconstruction error diverges exponentially for highly correlated systems if the mean transmittance T_0 remains constant. However, in chaotic scattering systems, T_0 and a are physically coupled; increasing the coupling strength typically enhances T_0 , which can offset the penalty from $J(a)$. The optimal design point emerges from this competition, as seen in Fig. 2(c) of the main text; it is the point where the gain in signal throughput (T_0^2) outweighs the exponential penalty from spectral correlations ($J(a)$).

In the under-determined case ($M < N$), the finite observation window modifies the effective correlation length. As derived in Sec. S3, the scaling function $\tilde{J}(a)$ incorporates a factor of $\sqrt{2}\beta$ (where $\beta = M/N < 1$) inside the hyperbolic sine term (Eq. 14).

Mathematically, this factor effectively reduces the rate of exponential growth compared to the over-determined case. Physically, this robustness arises from the spectral smoothing effect of the Fejér kernel (Bartlett windowing). By convolving the spectral density with the finite window, the deep spectral valleys (which correspond to near-zero eigenvalues) are broadened and lifted. This prevents the smallest eigenvalues from vanishing as rapidly as in the untruncated case, thereby suppressing the divergence of the pseudoinverse trace.

Fig. S2 illustrates the behavior of $J(a)$ and $\tilde{J}(a)$ across the full range of a , highlighting the universal baseline at $a = 0$ and the divergent behavior at large a .

S6. SUPER-RESOLUTION REGIME

In the main text, we defined the effective spectral resolution $\Delta\omega_{\text{min}}$ as the minimum frequency separation at which two spectral lines can be resolved with a reconstruction error below a threshold \mathcal{E}_{th} . In this section, we apply this definition to analyze the super-resolution regime $\Delta\omega_{\text{min}} < \Gamma_{\text{corr}}$.

Conventionally, the resolution of a speckle-based spectrometer is assumed to be limited by the spectral correlation width Γ_{corr} , analogous to the Rayleigh criterion in imaging. This heuristic states that spectral features separated by less than Γ_{corr} (the frequency scale over which speckles are highly correlated) cannot be distinguished. However, as indicated in Eq. 13 and Eq. 16 of the main text, this perspective overlooks the critical role of the signal-to-noise ratio. In the context of computational spectral reconstruction, “resolution” is not a hard physical barrier but a parameter estimation problem. Two spectral features separated by $\Delta\omega < \Gamma_{\text{corr}}$ can be resolved if the signal-to-noise ratio is sufficiently high to distinguish their slightly different “fingerprints”.

We illustrate this principle in Fig. S3(a)–(c). We consider an input spectrum consisting of discrete frequency comb lines separated by a spacing $\Delta\omega$. The transmission matrix A is simulated using the RMT model (see Sec. S2) with a correlation length significantly larger than the frequency channel spacing ($\Gamma_{\text{corr}} = 3\Delta\omega$). As shown in Fig. S3(a), the individual channels are spectrally overlapped within the correlation width. Using the same transmission matrix, we perform spectral reconstruction at two different noise levels, corresponding to different effective SNR values, \mathcal{R}_{SNR} , as defined in Eq. 13 of the main text. When the reconstruction is performed at $\mathcal{R}_{\text{SNR}} \approx 10^2$ [Fig. S3(b)], the algorithm fails to resolve individual lines, recovering only the broad envelope of the spectrum. The reconstruction error is high, and the effective resolution is coarse, consistent with the classical Γ_{corr} limit. At $\mathcal{R}_{\text{SNR}} \approx 10^7$ [Fig. S3(c)], however, the comb lines are resolved even though the scatterer remains identical. Evidently, sufficiently high \mathcal{R}_{SNR} allows the

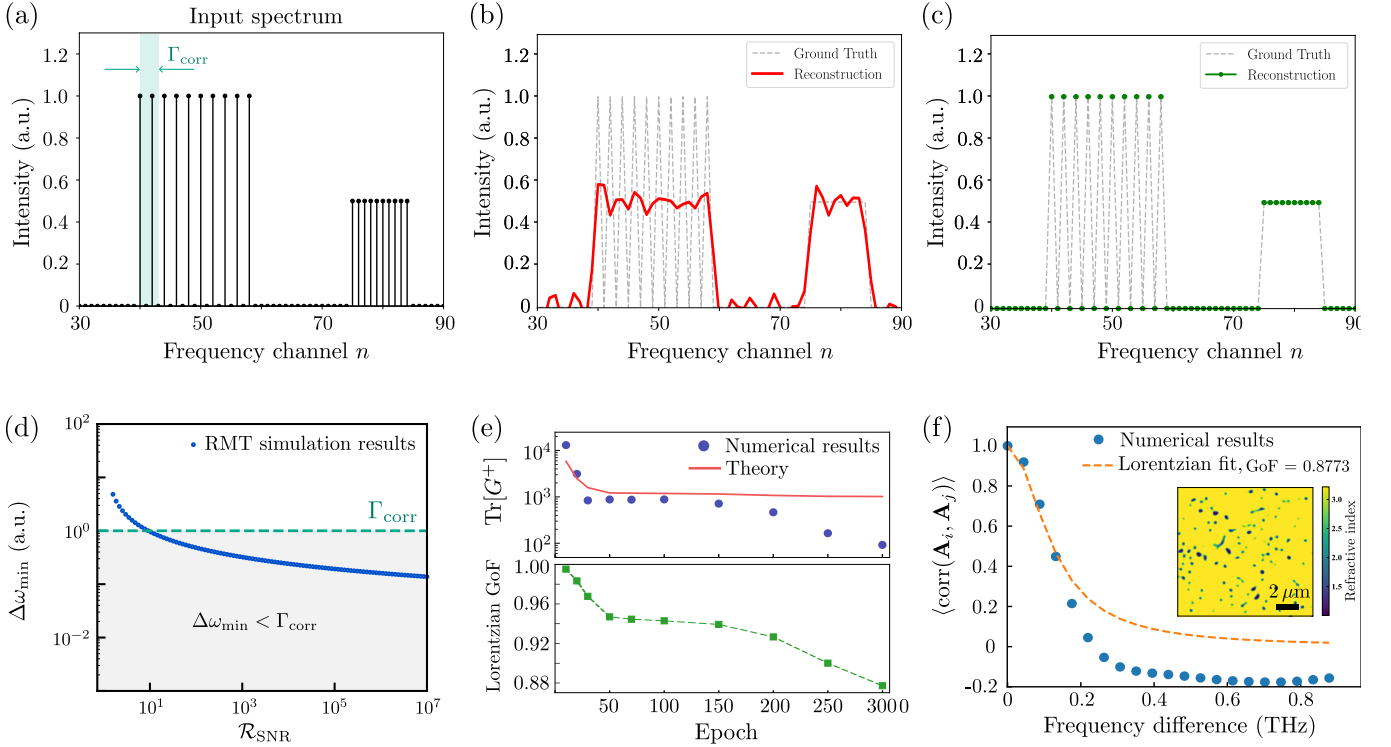


FIG. S3. (a) An input spectrum (black lines) consisting of $N = 100$ frequency channels spaced by $\Delta\omega$, where the spectral correlation width is $\Gamma_{\text{corr}} = 3\Delta\omega$ (green shaded region), implying strong spectral overlap. The number of detectors M is set to 150 to minimize the bias term. (b) Reconstruction result at $\mathcal{R}_{\text{SNR}} \approx 10^2$ (red line); the solver fails to resolve the individual comb lines in the actual spectrum (gray dashes). (c) Reconstruction result at $\mathcal{R}_{\text{SNR}} \approx 10^7$ using the same scatterer. The comb lines are now well-resolved (green circles). (d) Effective resolution $\Delta\omega_{\text{min}}$ (blue line) versus effective SNR \mathcal{R}_{SNR} calculated from Eq. 16, with $M = 150$ and $N = 100$. As \mathcal{R}_{SNR} increases, the resolution improves beyond the physical correlation limit Γ_{corr} (red dashed line), entering the super-resolution regime (gray shaded area). (e) Top panel: variation of $\text{Tr}[\mathbf{G}^+]$ (blue circles) and the corresponding theoretical prediction (red curve) versus number of optimization epochs, as a numerical inverse design scheme is employed to minimize $\text{Tr}[\mathbf{G}^+]$ in a full-wave FEM simulation. Bottom panel: the corresponding Lorentzian goodness-of-fit, defined as the Pearson correlation coefficient between the actual spectral correlation data and an ideal Lorentzian function with Γ_{corr} as the FWHM. (f) Spectral correlation function of the final optimized structure (blue circles) and the Lorentzian fit (orange dashes). Inset: the optimized refractive index distribution.

spectrometer to operate in the super-resolution regime.

Figure S3(d) quantifies this relationship. Based on the RMT simulations, we plot the theoretical resolution limit $\Delta\omega_{\text{min}}$ as a function of the effective SNR \mathcal{R}_{SNR} by varying the noise level σ_ϵ from 10^{-5} to 10^{-2} for 100 samples. The other system parameters are fixed at $M = 150$, $N = 100$, and $\delta_{th}^2 = 10^{-3}$. The dashed red line indicates the physical correlation limit Γ_{corr} , which is normalized to 1. As the SNR increases, $\Delta\omega_{\text{min}}$ decreases monotonically, eventually crossing below the Γ_{corr} threshold to enter the super-resolution regime.

S7. INVERSE DESIGN STUDY

As noted in the conclusion of our paper, it may be possible for individual extremal scatterers to surpass the performance bounds predicted by our theory, due to certain assumptions embedded in the theory. In particular, we have assumed that the scatterer obeys conventional speckle statistics with Lorentzian spectral correlations—which holds empirically for many real disordered scatterers and can be derived from RMT [20, 21, 32, 33], but is *not* immutable.

To study this issue, we conduct a full-wave FEM simulation study in which the structure is inverse-designed using the adjoint optimization method [39, 40], to minimize the variance bound $\text{Tr}[\mathbf{G}^+]$ [41]. In Fig. S3(e), the upper panel shows how $\text{Tr}[\mathbf{G}^+]$ varies with the number of optimization epochs (blue circles), along with the corresponding theoretical value calculated from Eq. (12) (red curve). The theory successfully tracks the actual decrease in $\text{Tr}[\mathbf{G}^+]$ for the first 100 or so epochs, but begins to fail after ~ 150 epochs. In the lower panel of Fig. S3(e), we see that this

failure coincides with a decrease in the goodness-of-fit to a Lorentzian spectral correlation function.

In Fig. S3(f), we plot the correlation function for the final optimized structure (whose refractive index is shown inset), which is indeed significantly non-Lorentzian. It thus appears that the $\text{Tr}[\mathbf{G}^+]$ minimization process works by introducing non-Lorentzian spectral correlations, moving the system away from the “fully developed speckle” regime—or, equivalently, altering the dwell-time distribution of the cavity eigenmodes.